

# Effect of Off-Diagonal Elements in Wannier Hamiltonian on DFT+DMFT: Study on the Low-Symmetry Material $\text{Li}_2\text{MnO}_3$

Alex Taekyung Lee

*Department of Chemical engineering, University of Illinois at Chicago, Chicago, IL 60608, USA and  
Materials Science Division, Argonne National laboratory, Lemont, IL 60439, USA*

Hyowon Park

*Department of Physics, University of Illinois at Chicago, Chicago, IL 60608, USA and  
Materials Science Division, Argonne National laboratory, Lemont, IL 60439, USA*

Anh T. Ngo\*

*Department of Chemical engineering, University of Illinois at Chicago, Chicago, IL 60608, USA and  
Materials Science Division, Argonne National laboratory, Lemont, IL 60439, USA*

(Dated: July 18, 2023)

We study the effect of the off-diagonal elements of the Wannier Hamiltonian on the electronic structure of low-symmetry material  $\text{Li}_2\text{MnO}_3$  ( $C2/m$ ), using dynamical mean field theory calculations with continuous-time Quantum Monte Carlo impurity solver. Presence of significant off-diagonal elements leads to a pronounced suppression of the energy gap. The off-diagonal elements are largest when the Wannier projection is used based on the global coordinate, and they remain substantial even with the projection using the local coordinate close to the direction of Mn-O bonds. We show that the energy gap is enhanced by the diagonalization of the Mn  $d$  block in the full  $p$ - $d$  Hamiltonian, with applying unitary rotation matrix. Additionally, the inclusion of a small double counting energy is crucial for achieving the experimental gap by reducing  $p$ - $d$  hybridization. Furthermore, we establish the efficiency of a low-energy ( $d$ -only basis) model for studying the electronic structure of  $\text{Li}_2\text{MnO}_3$ , as the Wannier basis represents a hybridized state of Mn  $d$  and O  $p$  orbitals. These findings suggest an appropriate approach for investigating low-symmetry materials using the DFT+DMFT method. To the best of our knowledge, no systematic study of the effect of off-diagonal terms has been conducted thus far. We also find that the antiferromagnetic ground state  $\Gamma_{2u}$  is stable with  $U \leq 2$  eV within density functional theory+ $U$  calculations, which is much smaller than widely used  $U=5$  eV.

PACS numbers:

## I. Introduction

Beyond density functional theory (DFT), dynamical mean field theory (DMFT) is one of the most successful method which account for the many-body correlation [1, 2]. In DMFT, the lattice problem is mapped onto an effective impurity problem, and solving this impurity model accurately is crucial for obtaining reliable results. Various impurity solvers have been developed [3], including Hirsh-Fye Quantum Monte Carlo (QMC) Method [4], continuous time quantum Monte Carlo (CTQMC) [2, 5, 6], exact diagonalization (ED) [3, 7], numerical renormalization group (NRG) [8], and density matrix renormalization group (DMRG) [9] methods.

Each method has advantages and disadvantages, and there is no method that provides the solution both accurately and efficiently, for all regimes of parameters. For example, ED solver does not have sign problem, but ED is computationally challenging if the number of bath sites needs to be increased [3]. Recently, CTQMC method has gained popularity as a solver for numerous DMFT appli-

cations, because it provides accurate solution over a wide range of parameter values. CTQMC also has a limitation, rooted in the sign problem. Specifically, to evade this issue, the off-diagonal elements of the Hamiltonian (or density matrix) are frequently omitted.

In the DFT+DMFT procedure [10], the Hamiltonian with a localized basis is obtained from the DFT calculations. A common approach involves the use of maximally localized Wannier functions [11]. However, to avoid the sign problem in CTQMC, only the diagonal elements of the Wannier Hamiltonian are considered for the many-body correlations. This becomes problematic when the point group symmetry of the transition metal (TM) ion is low, leading to significant mixing between  $d$  basis, and consequently, substantial off-diagonal elements in the Wannier Hamiltonian. Given that CTQMC only accounts for the diagonal elements, these large off-diagonal elements could contribute to considerable inaccuracies within DMFT calculations.

$\text{Li}_2\text{MnO}_3$ , one of the potential candidates for next generation cathode material due to the high voltage (4.4–5 V) and the low cost [12, 13], shows a good scenario for studying the impact of off-diagonal elements because of its low crystal symmetry.  $\text{Li}_2\text{MnO}_3$  has monoclinic structure with  $C/2m$  space group (No. 12). Since its six Mn-O

---

\*anhngo@uic.edu

bonds are neither parallel nor perpendicular (see Fig. 1), a substantial degree of mixing between the  $d$  orbitals is expected.

$\text{Li}_2\text{MnO}_3$  is an insulator with an experimental band gap ranging from 2.1 [14] to 2.17 eV [15]. The Mn ion in  $\text{Li}_2\text{MnO}_3$  exhibits a 4+ charge state ( $d^3$ ) and a high-spin configuration ( $S = 3/2$ ), resulting in a magnetic moment of 2.3–2.7  $\mu_B$  [16, 17]. In the high-spin state, the three  $d$  electrons fully occupy the spin-up  $t_{2g}$  band, leading to a non-zero gap for  $\text{Mn}^{4+}$  due to crystal field splitting and Hund coupling. At low temperatures,  $\text{Li}_2\text{MnO}_3$  exhibits an antiferromagnetic phase with a Néel temperature of  $T_N = 36\text{--}36.5$  K [16, 17]. Early studies of  $\text{Li}_2\text{MnO}_3$  reported the antiferromagnetic ground state to be  $\Gamma 3g$  with a magnetic propagation vector of  $Q_m = (0, 0, 0.5)$  [17]. However, recent studies have shown that the  $\Gamma_{2u}$  model with  $Q_m = (0, 0, 0.5)$  provides the best agreement with neutron diffraction data, while the  $\Gamma_{3g}$  model does not match the full refinement results [16].

Numerous studies based on density functional theory (DFT) have investigated the electronic and magnetic structures of  $\text{Li}_2\text{MnO}_3$  [13, 18–22]. However, a comprehensive understanding of these structures is still lacking. The band gaps have been predicted through various approaches such as DFT+ $U$  [18, 19], GW calculations [13], or hybrid functionals [13, 20]. Notably, previous studies have primarily focused on nonmagnetic [13, 22] or ferromagnetic [18–20] configurations, neglecting the magnetic ground state.

Understanding the paramagnetic phase of  $\text{Li}_2\text{MnO}_3$  holds great significance, particularly considering the operational temperature range of room temperature and the relatively low Néel temperature ( $T_N$ ) of  $\text{Li}_2\text{MnO}_3$  at 36 K [16]. However, conventional nonmagnetic calculations fail to accurately describe the paramagnetic spin order due to the absence of a local spin in the nonmagnetic phase, while the paramagnetic phase exhibits an averaged spin of zero due to the fluctuations of the local spin. To investigate the paramagnetic phase of  $\text{Li}_2\text{MnO}_3$ , recently developed DFT-based methods [23–25] or many-body techniques such as dynamical mean-field theory (DMFT) are required.

Other transition metal oxides for the cathode Li-ion batteries such as  $\text{LiCoO}_2$  [26] and  $\text{LiNiO}_2$  [27], which have higher symmetry ( $R\bar{3}m$ , No. 166), are also studied within DFT+DMFT. Interestingly, it has been shown that the electronic structure and the size of the energy gap in  $\text{LiNiO}_2$  strongly rely on the choice of the different Wannier basis [27]. Since the symmetry of  $\text{Li}_2\text{MnO}_3$  ( $C2/m$ ) is lower than the symmetry of  $\text{LiNiO}_2$  ( $R\bar{3}m$ ), the distortion of TM-O octahedron is larger in  $\text{Li}_2\text{MnO}_3$ . Consequently, the off-diagonal elements in  $\text{Li}_2\text{MnO}_3$  become more pronounced and play a crucial role. Therefore, a systematic study to examine the impact of these off-diagonal elements and the selection of various Wannier bases within the DFT+DMFT framework is needed for  $\text{Li}_2\text{MnO}_3$ .

In this study, we explore the influence of off-diagonal

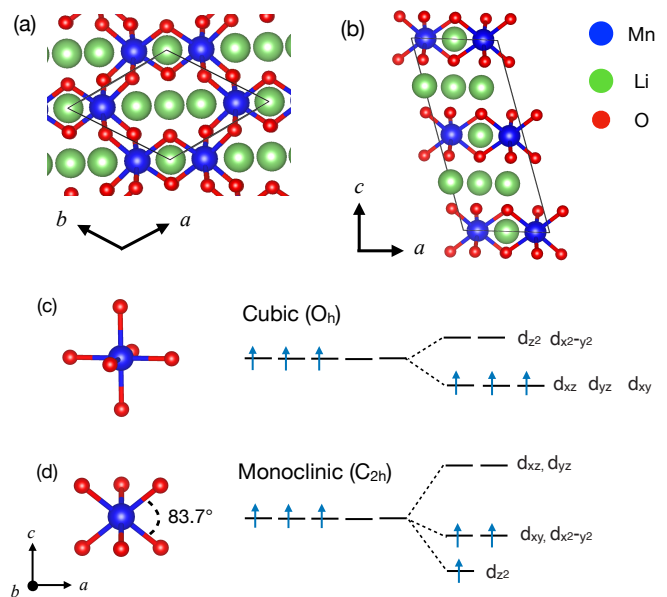


FIG. 1: (a) top and (b) side view for the atomic structure of  $\text{Li}_2\text{MnO}_3$ . Li atoms are located between  $\text{MnO}_3$  layers and the center of the hexagon. Schematic band splitting based on the (c) cubic ( $O_h$ ) and (d) monoclinic ( $C_{2h}$ ) crystal fields. Vectors  $\mathbf{a}$ ,  $\mathbf{b}$ , and  $\mathbf{c}$  indicate the global coordinates. Note that Mn-O bonds are the global axes are not parallel in the monoclinic phase.

elements in the Wannier Hamiltonian on the electronic structure of  $\text{Li}_2\text{MnO}_3$  using DFT+DMFT. The low symmetry of  $\text{Li}_2\text{MnO}_3$  ( $C2/m$ ) results in significant off-diagonal terms, leading to a suppressed energy gap within DMFT using  $U=5$  eV. Although a Wannier basis aligned with the local  $\text{MnO}_6$  coordinate reduces off-diagonal elements, they remain large, resulting in a suppressed gap due to the low point group symmetry. We apply a unitary rotation matrix to diagonalize the block diagonal part of the Mn  $d$  Hamiltonian to mitigate the effect. However, the resulting gap remains smaller than the experimental value, and increasing  $U$  does not resolve the discrepancy. We use a small double counting energy to obtain the experimental band gap, considering the influence of  $p$ - $d$  covalency. Additionally, we find that a minimal  $d$ -only Wannier basis efficiently captures the electronic structure by encompassing the hybridized states of Mn  $d$  and O  $p$  orbitals.

## II. Methods

### A. DFT+DMFT

We employ the non-charge-self-consistent DFT+DMFT method [10, 28] for relaxed structures obtained from DFT calculations. For DFT calculation, we use the projector augmented wave (PAW) method

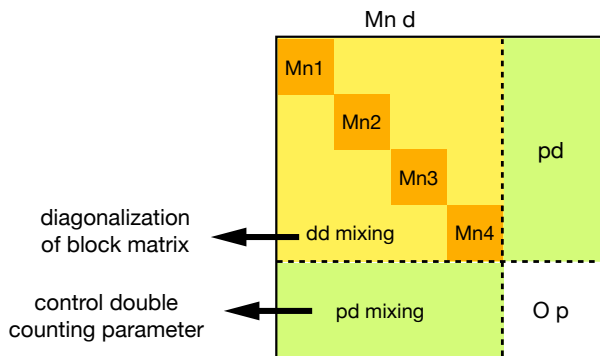


FIG. 2: Schematic diagram of the Wannier Hamiltonian matrix for Mn  $d$  and O  $p$  orbitals. We diagonalize the diagonal blocks of each Mn  $d$  states (orange boxes), and control  $p-d$  correlation by changing double counting parameter.

[29] and the revised version of the generalized gradient approximation (GGA) proposed by Perdew *et al.* (PBEsol) [30] as implemented in the VASP software [31]. Spin-independent version of the exchange correlation functional are employed. A plane wave basis with a kinetic energy cutoff of 500 eV is used. We used 24 atom unit cells (i.e.,  $1 \times 1 \times 2$  unit cells), which contains 4 Mn atoms, and  $\Gamma$ -centered  $\mathbf{k}$ -point meshes of size  $10 \times 10 \times 5$ . Atomic positions within the unit cells were relaxed until the residual forces were less than 0.01 eV/Å, and the stress was relaxed below 0.02 kB.

We solve the many-body problem on the manifold of both Mn  $3d+O p$  Wannier orbitals and Mn  $3d$ -only orbitals. The DFT+DMFT calculation has the following steps. First, we solve the non-spin-polarized Kohn-Sham (KS) equation within DFT using VASP. Second, we construct a localized-basis Hamiltonian for the Mn  $3d$  bands by generating maximally localized Wannier functions (MLWFs) [11] for the nonmagnetic DFT band structure. The energy window employed ranges from  $E_F - 9.0$  eV to  $E_F + 5.5$  eV for the  $pd$  basis, and  $E_F - 2.0$  eV to  $E_F + 4.0$  eV for the  $d$ -only basis. Finally, we solve the DMFT self-consistent equations for the correlated subspace of Mn  $3d$  and O  $p$  Wannier orbitals (or only Mn  $3d$  orbitals) using the continuous time quantum Monte Carlo (CTQMC) [2, 32] impurity solver.

Coulomb interaction element  $U_{m_4 m_3 m_2 m_1}$  in the Slater Hamiltonian using spherical harmonics function  $Y_{lm}$  is given by

$$U_{m_4 m_3 m_2 m_1} = \sum_k \frac{4\pi}{2k+1} F_l^k \langle Y_{lm_4} | Y_{k, m_4 - m_1} | Y_{lm_1} \rangle \times \langle Y_{lm_3} | Y_{k, m_2 - m_3}^* | Y_{lm_2} \rangle \quad (1)$$

where  $F^k$  are Slater integrals. Both Hubbard  $U$  and Hund's couplings  $J$  are parameterized by the Slater integrals, using  $U = F^0$  and  $J = (F^2 + F^4)/14$ . We consider full Coulomb interaction including density-density (where  $m_1 = m_4$  and  $m_2 = m_3$ ), spin-flip, and pair-

hopping terms. To study the effect of the off-diagonal elements of the Coulomb interaction matrix on the electronic structure, we also use only density-density interaction term and compare with the full Coulomb interaction calculations. We note that results using density-density approximation and full Coulomb interaction are qualitatively same (see Appendix A). For the  $pd$  basis Hamiltonian, we used  $U$  values of 5 and 7 eV and  $J$  of 0.9 eV. We used electronic temperatures of 300 K to study the temperature effect on the spectral function.

Within DFT+DMFT framework [10], the self-energy convergence is achieved when  $\Sigma^{\text{loc}}(i\omega) = \Sigma^{\text{imp}}(i\omega)$ , where  $\Sigma^{\text{loc}}(i\omega)$  and  $\Sigma^{\text{imp}}(i\omega)$  are local and lattice self-energies, respectively, and  $i\omega$  is imaginary frequency.  $\Sigma$  is approximated as a local quantity in the correlated subspace. DFT+DMFT total energy is given by

$$E^{\text{TOT}} = E^{\text{DFT}}(\rho) + \sum_{m, \mathbf{k}} \epsilon_m(\mathbf{k}) \cdot [n_{mm}(\mathbf{k}) - f_m(\mathbf{k})] + E^{\text{POT}} - E^{\text{DC}}, \quad (2)$$

where  $E^{\text{DFT}}$  is the total energy from non spin-polarized DFT, and  $\epsilon_m(\mathbf{k})$  are the DFT eigenvalues.  $n_{mm}(\mathbf{k})$  and  $f_m(\mathbf{k})$  are the diagonal DMFT occupancy matrix element and Fermi function, respectively, for  $m$ th KS band and momentum  $\mathbf{k}$ . The potential energy  $E^{\text{POT}}$  is calculated by using Migdal-Galiski formula [33]:

$$E^{\text{POT}} = \frac{1}{2} \sum_{\omega} [\Sigma^{\text{loc}}(i\omega) \cdot G^{\text{loc}}(i\omega)]. \quad (3)$$

Here, the local Green's function is simplified by  $G^{\text{loc}}(i\omega) = \sum_{\mathbf{k}} G^{\text{loc}}(\mathbf{k}, i\omega)$ .

To obtain the spectral function, the maximum entropy method is used for the analytic continuation. Spectral function  $A(\omega)$  is given by

$$A(\omega) = -\frac{1}{\pi} \text{Im} \left[ \sum_{\mathbf{k}} G^{\text{loc}}(\mathbf{k}, \omega) \right]. \quad (4)$$

### 1. Different Wannier basis and Diagonalization of the Wannier Hamiltonian

When investigating the electronic structure of  $\text{Li}_2\text{MnO}_3$  using the DMFT method, it is crucial to address two key issues: (i) the presence of significant off-diagonal terms in the Wannier Hamiltonian (yellow region in Fig. 2), and (ii) the significance of  $p-d$  correlation due to strong  $p-d$  hybridization (green region in Fig. 2). To overcome these challenges, we employed two strategies: (i) diagonalizing the block  $d$  Hamiltonian, and (ii) utilizing different values of double counting parameters, as summarized in Figure 2.

Large off-diagonal terms in the Hamiltonian can lead to significant errors within the DMFT method, as CTQMC only treats the diagonal terms to circumvent the sign problem. The non-parallel alignment of the cartesian

axes of the Wannier orbitals and the directions of the Mn-O bonds arises from the  $C_{2h}$  point group symmetry of the MnO6 octahedron. In cases where the point group symmetry of the transition metal (TM) octahedron is non-cubic, such as trigonal or monoclinic, there is a substantial mixing of the  $d$  basis ( $d_{xy}$ ,  $d_{xz}$ ,  $d_{yz}$ ,  $d_{z^2}$ ,  $d_{x^2-y^2}$ ), as these bases are defined within the cubic crystal field framework. Consequently, the off-diagonal terms of the Wannier Hamiltonian with the cubic  $d$  orbital basis become significant, leading to errors within the DMFT calculations. It is noteworthy that DFT+ $U$  does not encounter such issues since DFT+ $U$  exhibits rotational invariance [34], allowing for the inclusion of off-diagonal terms in the density matrix.

We employed three distinct approaches to investigate the impact of off-diagonal elements in  $\text{Li}_2\text{MnO}_3$ : (i) utilizing the global coordinate system, (ii) adopting the local Mn-O bond coordinate system, and (iii) diagonalizing the Mn  $d$  blocks (orange region in Fig. 2) of the Hamiltonian by applying a unitary rotation matrix. The selection of a suitable local coordinate system is not straightforward due to the non-perpendicular arrangement of Mn-O bonds, as depicted in Fig. 1(d). To address this, we designated the longest Mn-O bond as the local  $z$ -axis and established local  $x$ - and  $y$ -axes that were perpendicular to the  $z$ -axis. We then minimized the displacement between the real Mn-O bond and the local  $x$ - and  $y$ -axes.

## 2. Controlling $p$ - $d$ Covalency through Double Counting Energy

On the other hand, if  $p$  -  $d$  hybridization is strong as the nickelates [35, 36], applying nonzero  $U$  on  $p$  -  $d$  Wannier Hamiltonian may not capture the physics of  $pd$  correlation properly. To resolve this issue, we use the double counting parameter, which control the degree of  $p$  -  $d$  covalency. In term of double counting corrections for DFT+DMFT, we use a double counting energy ( $E^{\text{DC}}$ ) and potential ( $V^{\text{DC}} = \partial E^{\text{DC}} / \partial N_d$ ) similar to the conventional fully localized limit [28, 37]:

$$E^{\text{DC}} = \frac{U}{2} N_d \cdot (N_d - 1) - \frac{J}{4} N_d \cdot (N_d - 2), \quad (5)$$

$$V^{\text{DC}} = \frac{U}{2} \left( \bar{N}_d - \frac{1}{2} \right) - \frac{J}{2} (\bar{N}_d - 1) \quad (6)$$

Here  $\bar{N}_d = N_d - \alpha$ , where  $N_d$  is the  $d$  occupancy obtained self-consistently at each Mn site, and  $\alpha$  is double counting parameter.  $N_d$  is computed from the local Green function  $G^{\text{loc}}(\mathbf{k}, \mathbf{k}', i\omega)$ :

$$N_d = \sum_{a,\omega} \sum_{\mathbf{k}, \mathbf{k}'} \text{Im} \{ [\phi_d^a(\mathbf{k})]^* G^{\text{loc}}(\mathbf{k}, \mathbf{k}', i\omega) \phi_d^a(\mathbf{k}') \}, \quad (7)$$

where  $\phi_d^a(\mathbf{k})$  is the normalized  $d$ -orbital wavefunction, which is transformed from the wavefunction in the real

space  $\phi_d^a(\mathbf{r})$  with the center of coordinates  $\mathbf{r}$  on a transition metal ion. Note that  $\alpha = 0$  gives the conventional fully localized limit. From the Eqs. 5 and 6, changing  $\alpha$  (or  $V^{\text{DC}}$ ) can tune the  $p$ - $d$  covalency by effectively shifting the  $d$  orbital level. If  $V^{\text{DC}}$  potential is smaller than the DC potential of fully localized limit, it will make  $d$  orbital level higher and the covalency effect weaker, with reduced  $N_d$ .

## B. DFT+ $U$ and atomic structures

The GGA+ $U$  scheme within the rotationally invariant formalism together with the fully localized limit double-counting formula [34] is used to study the effect of electron interactions. We considered three different Hund's parameter ( $J$ ) values,  $J = 0, 0.5$ , and  $0.9$ . It is worth mentioning that when  $J = 0$ , the exchange interaction is already included in the spin-dependent DFT exchange-correlation potential, as demonstrated in a previous study [35]. While the consideration of the full Coulomb vertex is crucial in certain systems [38], the electronic structures of  $\text{Li}_2\text{MnO}_3$  obtained with non-zero  $J$  values are qualitatively similar to those obtained with  $J = 0$ , as detailed in Appendix B. The band gap is robust on  $J$ , while the larger values of  $J$  lead to an increased critical  $U$  value for the magnetic transition. Therefore, unless otherwise specified, we adopt  $J = 0$  throughout the manuscript.

Projected density of states (PDOS) are obtained by the spherical harmonic projections inside spheres around each atom. Wigner-Seitz radii of 1.323 Å were used for the projection of Mn atoms, respectively, as implemented in the VASP-PAW pseudopotential.

Both spin-independent and spin-dependent versions of the exchange correlation functional are employed in the DFT+ $U$  calculations. The structural relaxations, including the relaxation of internal forces and stress, were performed independently for each magnetic configuration, as well as for each value of  $U$  and  $J$ .

## III. Results and discussion

At low temperature,  $\text{Li}_2\text{MnO}_3$  is antiferromagnetic with  $T_N = 36\text{K}$  [16]. There are many DFT+ $U$  studies of  $\text{Li}_2\text{MnO}_3$ , using  $U(\text{Mn}) = 5\text{eV}$  [18-22], but the previous studies only considered nonmagnetic or ferromagnetic configuration. Therefore, in Section III A, we systematically study the electronic structures and magnetic stabilities of  $\text{Li}_2\text{MnO}_3$  using DFT and DFT+ $U$ .

In addition,  $\text{Li}_2\text{MnO}_3$  has paramagnetic spin configuration, which is not studied yet. In Section III B, we delve into the electronic structure of  $\text{Li}_2\text{MnO}_3$  within the DFT+DMFT method, enabling a systematic examination of the effects of off-diagonal terms in the Wannier Hamiltonian.

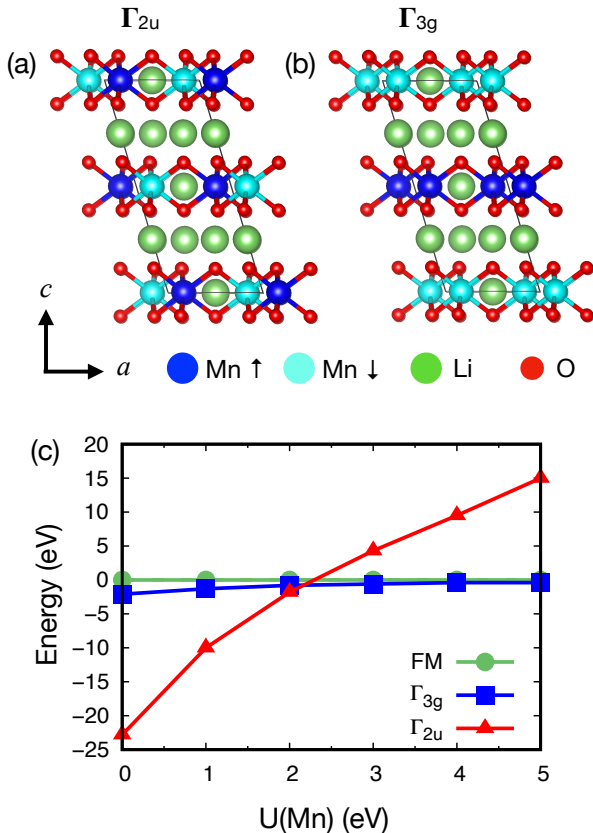


FIG. 3: Possible magnetic phases of  $\text{Li}_2\text{MnO}_3$  at low temperature, (a)  $\Gamma_{2u}$  and (b)  $\Gamma_{3g}$ . Mn ions with spin-up and spin-down are represented by different colors (blue and sky-blue). (c) the relative energies of the ferromagnetic,  $\Gamma_{2u}$ , and  $\Gamma_{3g}$  phases, as a function of  $U(\text{Mn})$ . Energy of the ferromagnetic phase is set to be zero.

### A. DFT+U

We begin the discussion by studying the magnetic phase of  $\text{Li}_2\text{MnO}_3$ .  $\text{Li}_2\text{MnO}_3$  is antiferromagnetic with Neel temperature of  $T_N = 36$  K, and the magnetic propagation vector is  $Q_m = (0, 0, 0.5)$  [17]. Earlier study suggested that  $\Gamma_{3g}$  is the ground state [17]. However, recent neutron diffraction study for both powder and single crystal showed that the ground state is  $\Gamma_{2u}$ , and  $\Gamma_{3g}$  model does not match with the experiment from the full refinement [16]. Magnetic moment of Mn is  $2.3\text{--}2.7 \mu_B$  [16, 17], indicating that Mn has high-spin state.

In Figure 3, we compare the energies of the ferromagnetic (FM), antiferromagnetic  $\Gamma_{3g}$  and  $\Gamma_{2u}$  phases, as a function of  $U(\text{Mn})$ .  $\Gamma_{2u}$  phase is most stable if  $U(\text{Mn}) \leq 2$ , while  $\Gamma_{3g}$  becomes more stable when  $U(\text{Mn}) > 2$  eV, while the Mn ion always has the high-spin state. This result shows that  $U(\text{Mn}) \leq 2$  eV is needed to obtain the experimental ground state. Previous linear response calculation for spinel  $\text{Mn}^{4+}$  suggested that  $U(\text{Mn}) = 5.04$  eV [39], and many DFT+U studies [18–22] used  $U(\text{Mn}) = 5$

eV based on this study.

However, it is important to note that using  $U$  values obtained from linear response theory within GGA+ $U$  can lead to an overestimation of correlation effects in transition metal oxides. This is typical in DFT+ $U$  since the Coulomb interaction is treated in a Hartree-Fock-like fashion, neglecting local correlation effects. For example, quantities such as bond length disproportionation can be overestimated using DFT+ $U$ , and this overestimation can be corrected by considering the local correlation effects through the use of DMFT [40]. In light of this, we suggest that for the study of electronic and magnetic properties of  $\text{Li}_2\text{MnO}_3$  within DFT+ $U$ , a reasonable value for  $U(\text{Mn})$  is 2 eV.

Interestingly, we find that the in-plane magnetic interaction in  $\text{Li}_2\text{MnO}_3$  is strong and sensitive to  $U$ , while the out-of-plane magnetic interaction is weak and less affected by  $U$ . Specifically, the energy difference between the ferromagnetic (FM) and  $\Gamma_{3g}$  antiferromagnetic phases,  $E[\text{FM}] - E[\Gamma_{3g}]$ , ranges from 2.1 to 0.4 eV as  $U$  varies from 0 to 5 eV. This indicates a preference for antiferromagnetic ordering in the out-of-plane direction, but with weak magnetic stability. On the other hand, the energy difference between the  $\Gamma_{3g}$  and  $\Gamma_{2u}$  antiferromagnetic phases,  $E[\Gamma_{3g}] - E[\Gamma_{2u}]$ , ranges from 20.7 to 15.4 meV for  $U = 0$  to 5 eV, indicating a stronger in-plane antiferromagnetic interaction.  $\text{Li}_2\text{MnO}_3$  is a layered material, with Li atoms located between the  $\text{MnO}_3$  layers, resulting in weak interlayer interactions between the  $\text{MnO}_3$  layers. It is worth noting that the shortest Mn-Mn distances in the in-plane and out-of-plane directions are 2.84 and 5.01 Å, respectively, which explains the strong in-plane and weak out-of-plane Mn-Mn interactions.

When  $U(\text{Mn}) \leq 2$  eV, the energy difference between  $\Gamma_{2u}$  and other magnetic configuration decreases as a function of  $U$ . With  $U(\text{Mn}) = 2$  eV,  $\Gamma_{2u}$  is more stable than FM and  $\Gamma_{3g}$  by 1.8 and 0.8 meV, respectively, consistent with the low Néel temperature  $T_N = 36$  K. Magnetic moment of Mn in  $\Gamma_{2u}$  phase is  $2.8 \mu_B$ , similar to the experimental value  $2.3 \mu_B$ .

Next, we study the effect of  $U$  on the electronic structure and energy gap of  $\text{Li}_2\text{MnO}_3$ . Mn ion in  $\text{Li}_2\text{MnO}_3$  has 4+ charge state with 3  $d$  electrons, and it has high-spin state.  $\text{MnO}_6$  in  $C2/m$  phase has  $C_{2h}$  point group symmetry, which splits the  $d$  bands into one lowest band ( $d_{z^2}$ ), double degenerate bands with higher energy ( $d_{xy}$  and  $d_{x^2-y^2}$ ), and highest energy bands ( $d_{xz}$  and  $d_{yz}$ ). As depicted in Fig. 1, three electrons of Mn occupy the three spin-up  $d_{z^2}$ ,  $d_{xy}$ , and  $d_{x^2-y^2}$  for the high-spin state. Therefore, there are two types of splittings which determine the energy gap ( $E_g$ ): (i) crystal field splitting ( $\Delta_{\text{CF}}$ ) between  $d_{xy} + d_{x^2-y^2}$  and  $d_{xz} + d_{yz}$  bands, and (ii) exchange splitting ( $\Delta_{\text{ex}}$ ) between spin-up  $d$  and spin-down  $d$  bands. These splittings are also presented in the PDOS in Fig. 4. We determine  $\Delta_{\text{CF}}$  and  $\Delta_{\text{ex}}$  by calculating the energy difference between the centers of the PDOS associated with each  $d$  band.

For the non-spin-polarized phase with  $U(\text{Mn}) = 0$ , the crystal field splitting ( $\Delta_{\text{CF}}$ ) is around 2.5 eV, while the exchange splitting ( $\Delta_{\text{ex}}$ ) is only about 0.6 eV. As a result, the band gap ( $E_g$ ) is almost zero, as depicted in Fig. 4(a). However, when spin polarization is introduced [Fig. 4(b)], the exchange splitting ( $\Delta_{\text{ex}}$ ) is significantly enhanced to approximately 2.2 eV, and the crystal field splitting ( $\Delta_{\text{CF}}$ ) also increases to around 3 eV. Since the exchange splitting ( $\Delta_{\text{ex}}$ ) determines the size of the energy gap ( $E_g$ ) due to  $\Delta_{\text{ex}} < \Delta_{\text{CF}}$ , the band gap ( $E_g$ ) becomes 1.19 eV.

With nonzero  $U$ , both the exchange splitting ( $\Delta_{\text{ex}}$ ) and the crystal field splitting ( $\Delta_{\text{CF}}$ ) increase, as shown in Fig. 4(c). With  $U(\text{Mn}) = 2$  eV, we obtain a band gap ( $E_g$ ) of 2.0 eV, which is in good agreement with the experimental gap of 2.1–2.17 eV [14, 15]. When  $U(\text{Mn}) = 5$  eV, the band gap ( $E_g$ ) is 1.9 eV, which is similar to the value obtained with  $U(\text{Mn}) = 2$  eV. While the occupied Mn  $d$  band is shifted to lower energies with a larger  $U$  value, the energy of the valence band maximum is less sensitive to  $U$ , resulting in minimal changes to the band gap ( $E_g$ ).

## B. DFT+DMFT

As discussed, the point group symmetry of  $\text{MnO}_6$  in  $\text{Li}_2\text{MnO}_3$  is  $C_{2h}$ , which is different from the cubic  $O_h$  symmetry. This is illustrated schematically in Figs. 1(c) and (d). In the cubic phase, the local Mn-O bonds align with the global coordinates based on the symmetry, resulting in a Hamiltonian based on the  $d$  orbitals without any off-diagonal terms. However, in the  $C_{2/m}$  phase, the local Mn-O axes and the global axes are not parallel. Therefore, if the global coordinates is used for the Wannier projection, significant off-diagonal terms emerge in the Hamiltonian, as shown in Eq. 8.

$\mathbf{H}_i =$

$$\begin{array}{c} d_{z^2} \quad d_{xz} \quad d_{yz} \quad d_{x^2-y^2} \quad d_{xy} \\ \begin{array}{c} d_{z^2} \\ d_{x^2-y^2} \\ d_{yz} \\ d_{x^2-y^2} \\ d_{xy} \end{array} \begin{pmatrix} 3.784 & 0.002 & 0 & -0.007 & 0 \\ 0.002 & 4.583 & 0 & \mathbf{-0.592} & 0 \\ 0 & 0 & 4.578 & 0 & \mathbf{0.584} \\ -0.007 & \mathbf{-0.592} & 0 & 4.153 & 0 \\ 0 & 0 & \mathbf{0.584} & 0 & 4.152 \end{pmatrix} \end{array} \quad (8)$$

Using this Hamiltonian, we employed DFT+DMFT calculations and plot the spectral functions in Fig. 5(a). Considering that the battery operates at room temperature, we set the temperature to 300 K. Since  $T_N = 65$  K of  $\text{Li}_2\text{MnO}_3$  is much lower than 300 K, we focus on the paramagnetic phase. When using the non-rotated basis in the DMFT calculations, the resulting energy gap ( $E_g$ ) is only 0.4 eV, significantly smaller than the experimental value.

To mitigate the large error of  $E_g$  caused by the signifi-

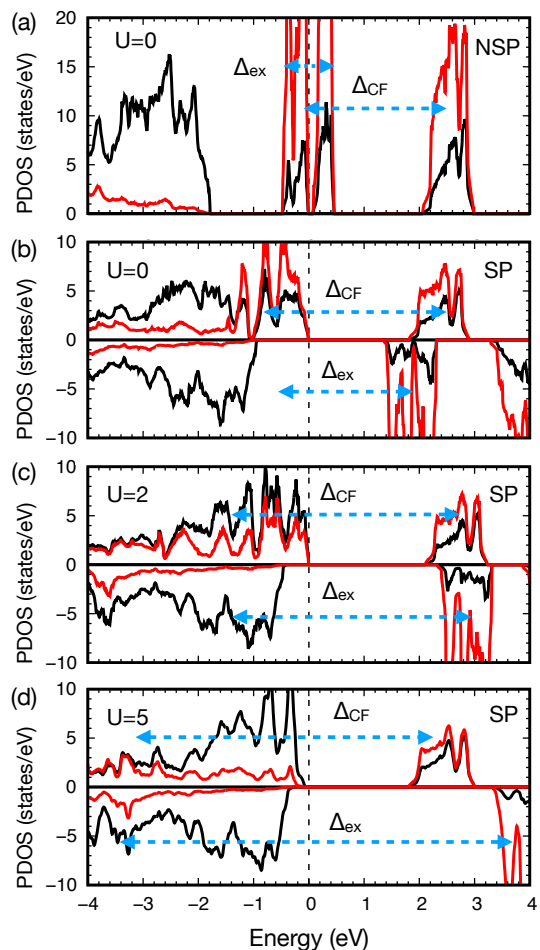


FIG. 4: Projected density of states (PDOS) onto the Mn  $d$  (red) and O  $p$  (black) in  $\text{Li}_2\text{MnO}_3$ . (a)  $U(\text{Mn}) = 0$  for non spin-polarized configuration, (b)  $U(\text{Mn}) = 0$  for spin-polarized configuration (ferromagnetic), (c)  $U(\text{Mn}) = 2$  and (d)  $U(\text{Mn}) = 5$  for spin-polarized configuration. The length of the arrows ( $\Delta_{\text{ex}}$  and  $\Delta_{\text{CF}}$ ) are serves as a guide for the eyes.

cant off-diagonal terms, we also employed the local coordinate system by using different Wannier basis that minimize the magnitude of the off-diagonal elements. The selection of the local coordinate system is described in detail in Section II A 2.

$\mathbf{H}_{\text{rot}} =$

$$\begin{array}{c} d_{z^2} \quad d_{xz} \quad d_{yz} \quad d_{x^2-y^2} \quad d_{xy} \\ \begin{array}{c} d_{z^2} \\ d_{xz} \\ d_{yz} \\ d_{x^2-y^2} \\ d_{xy} \end{array} \begin{pmatrix} 4.069 & 0.018 & -0.009 & \mathbf{-0.530} & 0.059 \\ 0.018 & 3.775 & 0.064 & 0.010 & 0.003 \\ -0.009 & 0.064 & 4.997 & -0.011 & 0.006 \\ \mathbf{-0.530} & 0.010 & -0.011 & 4.668 & -0.101 \\ 0.059 & 0.003 & 0.006 & -0.101 & 3.754 \end{pmatrix} \end{array} \quad (9)$$

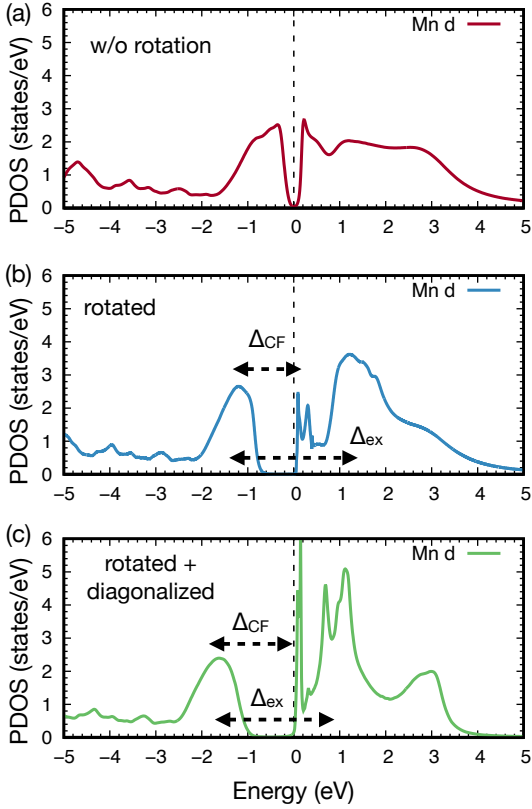


FIG. 5: DFT+DMFT spectral functions of Mn  $d$  Wannier orbitals, with  $pd$  model. (a) global coordinate is used for Wannier projection, (b) local coordinate obtained by unitary rotation matrix is used for Wannier projection, and (c) block diagonal part of Mn  $d$  Hamiltonian is diagonalized. The calculations use  $U = 5$  eV,  $J = 0.9$  eV, and a temperature of 300 K. The length of the arrows ( $\Delta_{ex}$  and  $\Delta_{CF}$ ) are serves as a guide for the eyes.

As shown in Eq. 9, the off-diagonal terms are significantly reduced, leading to an increase in  $E_g$  to 0.6 eV. However, the obtained value of  $E_g$  is still significantly smaller than the experimental gap. As depicted in Fig. 5(b), the underestimation of  $E_g$  can be attributed to the small value of  $\Delta_{CF}$ .  $\Delta_{CF}$  within DMFT with rotated Wannier axes is around 1.5 eV, which is considerably smaller than the value within DFT+ $U$  ( $\sim 3$  eV). In contrast,  $\Delta_{ex}$  is approximately 2.7 eV and has a negligible effect on  $E_g$ .

To resolve the underestimation of  $E_g$  within DFT+DMFT, we diagonalize each Mn  $d$  block of the Hamiltonian (orange boxes in Fig. 2), which can be obtained by the unitary rotation matrix. Diagonalized

Wannier Hamiltonian is shown in Eq. 10.

$$\mathbf{H}_{dia} = \begin{matrix} & d_{z^2} & d_{xz} & d_{yz} & d_{x^2-y^2} & d_{xy} \\ \begin{matrix} d_{z^2} \\ d_{xz} \\ d_{yz} \\ d_{x^2-y^2} \\ d_{xy} \end{matrix} & \begin{pmatrix} 3.745 & 0 & 0 & 0 & 0 \\ 0 & 3.788 & 0 & 0 & 0 \\ 0 & 0 & 4.998 & 0 & 0 \\ 0 & 0 & 0 & 4.985 & 0 \\ 0 & 0 & 0 & 0 & 3.741 \end{pmatrix} \end{matrix} \quad (10)$$

As presented in Fig. 5(b),  $E_g$  within DMFT is increased to 0.8 eV. However, this value is still smaller than the experimental gap. In order to further investigate this discrepancy, we explore different values of  $U$  and the double counting parameter  $\alpha$  using the diagonalized Hamiltonian (see Eq. 6). Surprisingly, we observe that both  $\Delta_{CF}$  and the resulting  $E_g$  are not significantly affected by variations in  $U$ . As shown in Fig. 6, the values of  $E_g$  with  $U=5$  and 7 are 0.8 and 0.9 eV, respectively.

In contrast, we find that both  $\Delta_{CF}$  and the resulting  $E_g$  are more sensitive to  $\alpha$ . For instance, when  $U=5$  eV, the value of  $E_g$  increases to 1.4 eV for  $\alpha = 0.8$ . Furthermore, for  $\alpha = 0.8$ , increasing  $U$  from 5 to 7 eV further enhances  $E_g$  from 1.4 to 2.0 eV. The sensitivity of the band gap  $E_g$  to  $\alpha$  suggests the importance of  $p$ - $d$  correlation ( $U_{pd}$ ) in determining  $\Delta_{CF}$ , due to the strong Mn  $d$ -O  $p$  hybridization in  $\text{Li}_2\text{MnO}_3$ . It is important to note that that modifying  $U_{dd}$  alone for the  $pd$  model Hamiltonian is insufficient, as it primarily affects the  $d$ - $d$  correlation without adequately addressing the  $p$ - $d$  covalency. Therefore, considering both  $d$ - $d$  and  $p$ - $d$  correlations is crucial for a comprehensive understanding of the electronic structure of  $\text{Li}_2\text{MnO}_3$ .

It should be noted that the off-diagonal elements of the local Green's function can remain small, regardless of the basis function. To study this, we examine both the diagonal and off-diagonal components of hybridization function obtained using global coordinate projection, local coordinate projection, and diagonalized Wannier Hamiltonian. The hybridization function is defined as

$$\hat{\Delta}(\omega) = (\omega + \mu)\hat{I} - \epsilon_{imp} - \hat{\Sigma}(\omega) - \left[ G^{cor}(\omega) \right]^{-1} \quad (11)$$

where  $\epsilon_{imp}$  is the matrix representing the impurity levels of correlated orbitals, and  $G^{cor}$  is correlated Green's function [10]. For each correlated atom, the hybridization function has a matrix form  $\Delta_{ij}$ , where  $i$  and  $j$  are orbital indices (5  $d$  orbitals). We define the diagonal elements of the hybridization function as  $\Delta_i^{dia} = |\Delta_{ii}|$  ( $i=1$  to 5), and the off-diagonal elements are defined by  $\Delta_i^{off} = \sum_{j \neq i} |\Delta_{ij}|/4$ . We compare the imaginary part of the diagonal and off-diagonal element, i.e.,  $Im(\Delta_i^{dia})$  and  $Im(\Delta_i^{off})$ . As presented in in Figure 7, the diagonal terms are much larger than the off-diagonal terms,  $\Delta_i^{off}$ . regardless of the Wannier projection and the diagonalization of the Wannier Hamiltonian. The use of

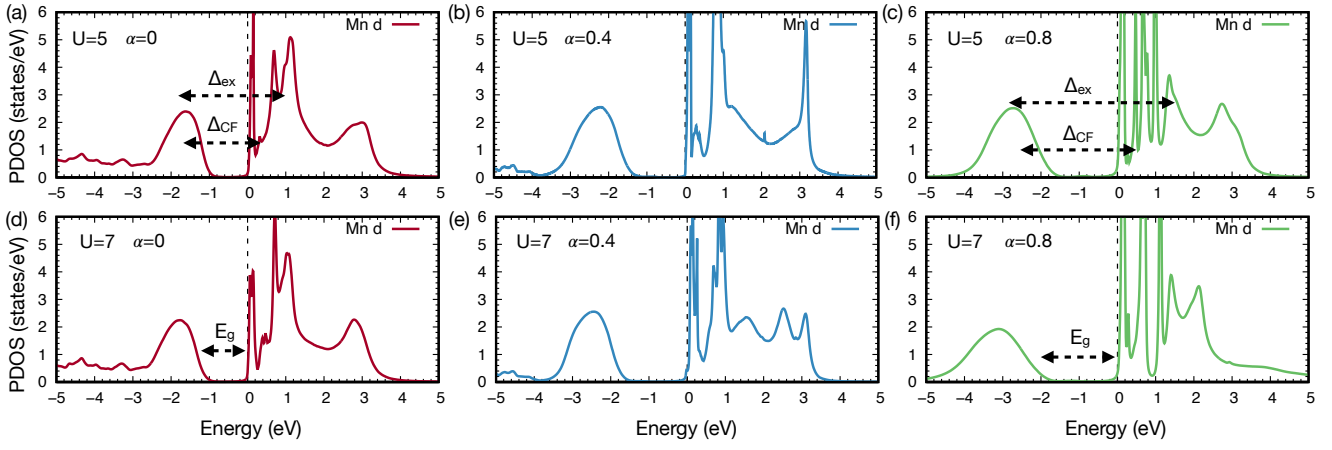


FIG. 6: DFT+DMFT spectral functions of Mn  $d$  Wannier orbitals with different  $U$  and  $\alpha$ . The calculations use temperature of 300 K. The length of the arrows ( $\Delta_{ex}$ ,  $\Delta_{CF}$ , and the energy gap  $E_g$ ) serves as a guide for the eyes.

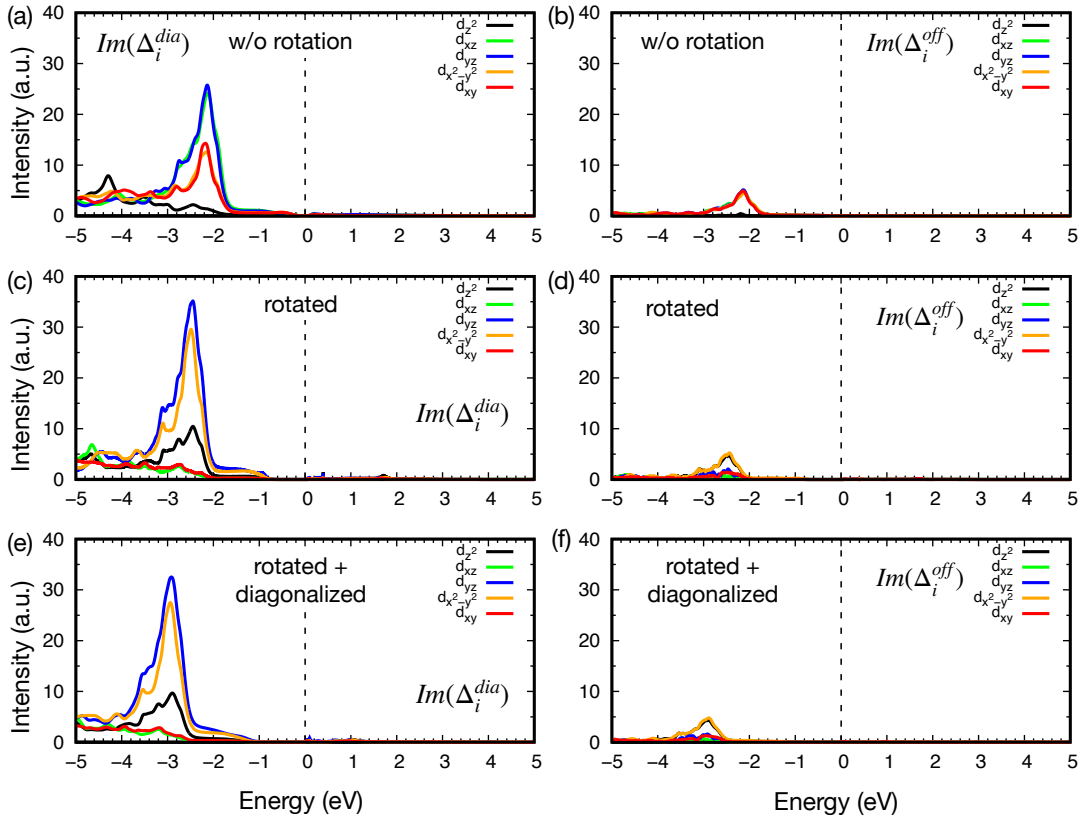


FIG. 7: (a), (c), and (e) diagonal elements of the hybridization function, and (b), (d), and (f) off-diagonal elements of the hybridization function. (a), (b) global coordinate is used for Wannier projection, (c), (d) local coordinate obtained by unitary rotation matrix is used for Wannier projection, and (e), (f) block diagonal part of Mn  $d$  Hamiltonian is diagonalized. The calculations use  $U = 5$  eV,  $J = 0.9$  eV, and a temperature of 300 K.

different basis functions leads to energy shift of the peak for the diagonal part of the hybridization function,  $\Delta_i^{dia}$ . Note that the real part of the hybridization function has

similar trend; diagonal term is also dominant.

Since both  $d$ - $d$  and  $p$ - $d$  correlations are important on the  $E_g$ , we also consider the  $d$ -only model Hamiltonian as an alternative approach to describe the electronic struc-

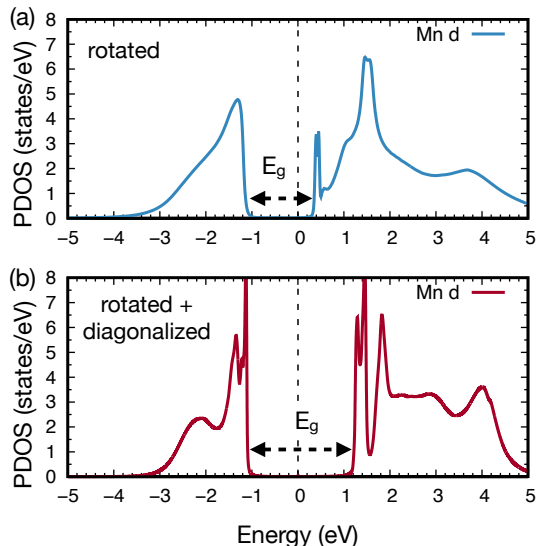


FIG. 8: DFT+DMFT spectral functions of Mn  $d$  Wannier orbitals with  $d$ -only model. (a) local coordinate obtained by unitary rotation matrix is used for Wannier projection, and (b) block diagonal part of Mn  $d$  Hamiltonian is diagonalized. The calculations use  $U = 2.0$  eV,  $J = 0.9$  eV, and a temperature of 300 K. The length of the arrows ( $E_g$ ) serves as a guide for the eyes.

ture of  $\text{Li}_2\text{MnO}_3$ . In the  $d$ -only model, the Wannier  $d$  orbitals represent the hybridized Mn  $d$  and O  $p$  orbitals, in contrast to the  $pd$  model where they closely resemble the Mn  $d$  orbital. Therefore, the effect of  $U(\text{Mn})$  on the  $d$ -only Wannier Hamiltonian is similar to the combined effects of  $U_{dd}$  and  $U_{pd}$  in the  $p-d$  model Hamiltonian. As a result, both  $\Delta_{CF}$  and  $E_g$  are sensitive to  $U(\text{Mn})$  within the  $d$ -only model. By employing Wannier projection with local coordinates, we obtain  $E_g$  of 1.3 eV with  $U(\text{Mn}) = 2.0$  eV, as shown in Fig. 8(a). Similarly to the  $pd$  basis, the diagonalization of the Wannier Hamiltonian further enhances  $E_g$ . In this case, the resulting  $E_g$  value becomes comparable to  $U(\text{Mn})$ , yielding  $E_g = 2.1$  eV with  $U(\text{Mn}) = 2.0$  eV, as presented in Fig. 8(b).

#### IV. Summary

In this work, we show that the off-diagonal terms of Mn  $d$  Hamiltonian and  $p-d$  interaction play crucial role on the electronic structure of  $\text{Li}_2\text{MnO}_3$ , through DFT+DMFT calculations. Our results highlight the significance of considering the off-diagonal terms in the Mn  $d$  block of the Wannier Hamiltonian, as treating only the diagonal terms in the CTQMC solver leads to a substantial impact on the electronic structure. The monoclinic symmetry ( $C2/m$ ) of  $\text{Li}_2\text{MnO}_3$  results in large off-diagonal terms in the Mn  $d$  block when using the global coordinate, leading to a significant suppression of the energy gap compared to the experimental value. By adopting a

local coordinate, the magnitude of the off-diagonal terms can be reduced, resulting in a substantial increase in the band gap, although it remains smaller than the experimental value.

To address this limitation, we diagonalize the Mn  $d$  block of the Wannier Hamiltonian by applying a unitary rotation matrix, leading to a further enhancement of the energy gap. However, even with this approach, the energy gap is still not large enough. We find that the strong hybridization between Mn  $d$  and O  $p$  necessitates considering the  $p-d$  correlation through the adjustment of the double counting parameter, in addition to increasing  $U_{dd}$ . In support of this concept, we also explore a  $d$ -only model Hamiltonian, which captures the hybridized state of the Mn  $d$  and O  $p$  orbitals. Our findings demonstrate the sensitivity of the energy gap to  $U$ , highlighting the importance of both  $dd$  and  $pd$  correlations in the electronic structure of  $\text{Li}_2\text{MnO}_3$ .

These findings suggest an appropriate approach for investigating low-symmetry materials using the DFT+DMFT method. To the best of our knowledge, no systematic study of the effect of off-diagonal terms has been conducted thus far. Moreover, we found that the magnetic ground state of  $\text{Li}_2\text{MnO}_3$  strongly depends on the choice of  $U$ . While the antiferromagnetic states ( $\Gamma_{2u}$  or  $\Gamma_{3g}$ ) are more stable than the ferromagnetic state in the wide range of  $U$  ( $U \leq 5$ ), experimentally observed ground state  $\Gamma_{2u}$  phase is most stable with  $U \leq 2$ . Hence, careful consideration of  $U$  is essential for future DFT+ $U$  studies of  $\text{Li}_2\text{MnO}_3$ .

## V. Acknowledgments

This research is supported by the Vehicle Technologies Office (VTO), Department of Energy (DOE), USA, through the Battery Materials Research (BMR) program. We also acknowledge financial support from the U.S.

Department of Energy, Office of Science, Office of Basic Energy Sciences, Materials Science and Engineering Division. We gratefully acknowledge the computing resources provided on Bebop, a high-performance computing cluster operated by the Laboratory Computing Resource Center at the Argonne National Laboratory.

- 
- [1] G. Kotliar, S. Y. Savrasov, K. Haule, V. S. Oudovenko, O. Parcollet, and C. A. Marianetti, *Rev. Mod. Phys.* **78**, 865 (2006), URL <https://link.aps.org/doi/10.1103/RevModPhys.78.865>.
- [2] K. Haule, *Phys. Rev. B* **75**, 155113 (2007), URL <https://link.aps.org/doi/10.1103/PhysRevB.75.155113>.
- [3] A. Georges, G. Kotliar, W. Krauth, and M. J. Rozenberg, *Rev. Mod. Phys.* **68**, 13 (1996), URL <https://link.aps.org/doi/10.1103/RevModPhys.68.13>.
- [4] J. E. Hirsch and R. M. Fye, *Phys. Rev. Lett.* **56**, 2521 (1986), URL <https://link.aps.org/doi/10.1103/PhysRevLett.56.2521>.
- [5] E. Gull, P. Werner, O. Parcollet, and M. Troyer, *Europhysics Letters* **82**, 57003 (2008), URL <https://dx.doi.org/10.1209/0295-5075/82/57003>.
- [6] E. Gull, A. J. Millis, A. I. Lichtenstein, A. N. Rubtsov, M. Troyer, and P. Werner, *Rev. Mod. Phys.* **83**, 349 (2011), URL <https://link.aps.org/doi/10.1103/RevModPhys.83.349>.
- [7] M. Caffarel and W. Krauth, *Phys. Rev. Lett.* **72**, 1545 (1994), URL <https://link.aps.org/doi/10.1103/PhysRevLett.72.1545>.
- [8] R. Bulla, *Phys. Rev. Lett.* **83**, 136 (1999), URL <https://link.aps.org/doi/10.1103/PhysRevLett.83.136>.
- [9] S. R. White, *Phys. Rev. Lett.* **69**, 2863 (1992), URL <https://link.aps.org/doi/10.1103/PhysRevLett.69.2863>.
- [10] V. Singh, U. Herath, B. Wah, X. Liao, A. H. Romero, and H. Park, *Computer Physics Communications* **261**, 107778 (2021), ISSN 0010-4655, URL <http://www.sciencedirect.com/science/article/pii/S001046552030388X>.
- [11] N. Marzari, A. A. Mostofi, J. R. Yates, I. Souza, and D. Vanderbilt, *Rev. Mod. Phys.* **84**, 1419 (2012), URL <https://link.aps.org/doi/10.1103/RevModPhys.84.1419>.
- [12] N. Yabuuchi, K. Yoshii, S.-T. Myung, I. Nakai, and S. Komaba, *Journal of the American Chemical Society* **133**, 4404 (2011), pMID: 21375288, <https://doi.org/10.1021/ja108588y>, URL <https://doi.org/10.1021/ja108588y>.
- [13] D.-H. Seo, J. Lee, A. Urban, R. Malik, S. Kang, and G. Ceder, *Nature Chemistry* **8**, 692 (2016), URL <https://doi.org/10.1038/nchem.2524>.
- [14] S. Tamilarasan, S. Laha, S. Natarajan, and J. Gopalakrishnan, *J. Mater. Chem. C* **3**, 4794 (2015), URL <http://dx.doi.org/10.1039/C5TC00616C>.
- [15] B. Singh and P. Singh, *SN Applied Sciences* **2**, 506 (2020), ISSN 2523-3971, URL <https://doi.org/10.1007/s42452-020-2260-z>.
- [16] S. Lee, S. Choi, J. Kim, H. Sim, C. Won, S. Lee, S. A. Kim, N. Hur, and J.-G. Park, *Journal of Physics: Condensed Matter* **24**, 456004 (2012), URL <https://dx.doi.org/10.1088/0953-8984/24/45/456004>.
- [17] P. Strobel and B. Lambert-Andron, *Journal of Solid State Chemistry* **75**, 90 (1988), ISSN 0022-4596, URL <https://www.sciencedirect.com/science/article/pii/0022459688903052>.
- [18] R. Xiao, H. Li, and L. Chen, *Chemistry of Materials* **24**, 4242 (2012), URL <https://doi.org/10.1021/cm3027219>.
- [19] S. Wang, J. Liu, and Q. Sun, *J. Mater. Chem. A* **5**, 16936 (2017), URL <http://dx.doi.org/10.1039/C7TA04941B>.
- [20] H. Chen and M. S. Islam, *Chemistry of Materials* **28**, 6656 (2016), URL <https://doi.org/10.1021/acs.chemmater.6b02870>.
- [21] Z. Chen, J. Li, and X. C. Zeng, *Journal of the American Chemical Society* **141**, 10751 (2019), pMID: 31251049, <https://doi.org/10.1021/jacs.9b03710>, URL <https://doi.org/10.1021/jacs.9b03710>.
- [22] K. Hikima, K. Shimizu, H. Kiuchi, Y. Hinuma, K. Suzuki, M. Hirayama, E. Matsubara, and R. Kanno, *Journal of the American Chemical Society* **144**, 236 (2022), pMID: 34957828, <https://doi.org/10.1021/jacs.1c09087>, URL <https://doi.org/10.1021/jacs.1c09087>.
- [23] D. Gambino, O. I. Mal'yi, Z. Wang, B. Alling, and A. Zunger, *Phys. Rev. B* **106**, 134406 (2022), URL <https://link.aps.org/doi/10.1103/PhysRevB.106.134406>.
- [24] G. Trimarchi, Z. Wang, and A. Zunger, *Phys. Rev. B* **97**, 035107 (2018), URL <https://link.aps.org/doi/10.1103/PhysRevB.97.035107>.
- [25] J. Du, O. Mal'yi, S.-L. Shang, Y. Wang, X.-G. Zhao, F. Liu, A. Zunger, and Z.-K. Liu, *Materials Today Physics* **27**, 100805 (2022), ISSN 2542-5293, URL <https://www.sciencedirect.com/science/article/pii/S2542529322002036>.
- [26] E. B. Isaacs and C. A. Marianetti, *Phys. Rev. B* **102**, 045146 (2020), URL <https://link.aps.org/doi/10.1103/PhysRevB.102.045146>.
- [27] D. M. Korotin, D. Novoselov, and V. I. Anisimov, *Phys. Rev. B* **99**, 045106 (2019), URL <https://link.aps.org/doi/10.1103/PhysRevB.99.045106>.
- [28] H. Park, R. Nanguneri, and A. T. Ngo, *Phys. Rev. B* **101**, 195125 (2020), URL <https://link.aps.org/doi/10.1103/PhysRevB.101.195125>.
- [29] P. E. Blöchl, *Phys. Rev. B* **50**, 17953 (1994), URL <http://link.aps.org/doi/10.1103/PhysRevB.50.17953>.
- [30] J. P. Perdew, A. Ruzsinszky, G. I. Csonka, O. A. Vydrov, G. E. Scuseria, L. A. Constantin, X. Zhou, and K. Burke, *Phys. Rev. Lett.* **100**, 136406 (2008), URL <http://link.aps.org/doi/10.1103/PhysRevLett.100.136406>.
- [31] G. Kresse and D. Joubert, *Phys. Rev. B* **59**, 1758 (1999), URL <http://link.aps.org/doi/10.1103/PhysRevB.59.1758>.
- [32] E. Gull, A. J. Millis, A. I. Lichtenstein, A. N. Rubtsov,

- M. Troyer, and P. Werner, Rev. Mod. Phys. **83**, 349 (2011), URL <https://link.aps.org/doi/10.1103/RevModPhys.83.349>.
- [33] V. Galitskii and A. Migdal, me Teoret. Fiz **34** (1958).
- [34] A. I. Liechtenstein, V. I. Anisimov, and J. Zaanen, Phys. Rev. B **52**, R5467 (1995), URL <http://link.aps.org/doi/10.1103/PhysRevB.52.R5467>.
- [35] H. Park, A. J. Millis, and C. A. Marianetti, Phys. Rev. B **92**, 035146 (2015), URL <http://link.aps.org/doi/10.1103/PhysRevB.92.035146>.
- [36] H. Park, A. J. Millis, and C. A. Marianetti, Phys. Rev. Lett. **109**, 156402 (2012), URL <https://link.aps.org/doi/10.1103/PhysRevLett.109.156402>.
- [37] V. I. Anisimov, J. Zaanen, and O. K. Andersen, Phys. Rev. B **44**, 943 (1991), URL <https://link.aps.org/doi/10.1103/PhysRevB.44.943>.
- [38] F. Bultmark, F. Cricchio, O. Grånäs, and L. Nordström, Phys. Rev. B **80**, 035121 (2009), URL <https://link.aps.org/doi/10.1103/PhysRevB.80.035121>.
- [39] F. Zhou, M. Cococcioni, C. A. Marianetti, D. Morgan, and G. Ceder, Phys. Rev. B **70**, 235121 (2004), URL <https://link.aps.org/doi/10.1103/PhysRevB.70.235121>.
- [40] H. Park, A. J. Millis, and C. A. Marianetti, Phys. Rev. B **90**, 235103 (2014), URL <https://link.aps.org/doi/10.1103/PhysRevB.90.235103>.

### A. Effect of the Coulomb interaction

The rotationally invariant Coulomb interaction in the form of the Slater-Kanamori interaction Hamiltonian is

$$\begin{aligned} \hat{H}_K = & U \sum_{\alpha} \hat{n}_{\alpha\uparrow} \hat{n}_{\alpha\downarrow} + \frac{1}{2} \sum_{\alpha \neq \beta} \sum_{\sigma \sigma'} (U' - J \delta_{\sigma \sigma'}) \hat{n}_{\alpha\sigma} \hat{n}_{\beta\sigma'} \\ & - \sum_{\alpha \neq \beta} \left( J c_{\alpha\uparrow}^{\dagger} c_{\alpha\downarrow} c_{\beta\downarrow}^{\dagger} c_{\beta\uparrow} + J' c_{\beta\uparrow}^{\dagger} c_{\beta\downarrow}^{\dagger} c_{\alpha\uparrow} c_{\alpha\downarrow} \right) \end{aligned} \quad (\text{A1})$$

Here  $c_{\sigma}$  and  $c_{\sigma}^{\dagger}$  denote the fermion annihilation and creation operators, where  $\sigma$  is spin.  $U$  is intra-orbital

density-density interaction parameter,  $U'$  is inter-orbital density-density interaction parameter,  $J$  is spin-flip interaction parameter, and  $J'$  is pair-hopping interaction parameter.

$U$ ,  $U'$ ,  $J$ , and  $J'$  are given by the matrix elements

$$\begin{aligned} U &= \left\langle \alpha\alpha \left| \frac{1}{r_{12}} \right| \alpha\alpha \right\rangle, \quad U' = \left\langle \alpha\beta \left| \frac{1}{r_{12}} \right| \alpha\beta \right\rangle \\ J &= \left\langle \alpha\beta \left| \frac{1}{r_{12}} \right| \beta\alpha \right\rangle, \quad J' = \left\langle \alpha\alpha \left| \frac{1}{r_{12}} \right| \beta\beta \right\rangle \end{aligned} \quad (\text{A2})$$

where  $U' = U - 2J$ ,  $J' = J$  due to the rotational invariance.

In Figure 9 we compare the spectral functions using full Coulomb interaction parameterized by Slater integral, including density-density, spin-flip, and pair-hopping interactions. We also used only the density-density interaction term (density-density approximation), and compared with the full Coulomb vertex calculation. Results are qualitatively similar, while the energy gap is reduced with full interaction for the global coordinate Wannier projection.

### B. DFT+ $U$ with nonzero $J$

In Figure 10, we compare the electronic structures using nonzero  $J = 0.5$  and  $0.9$ , and also compute the relative energies of the different magnetic configurations. We note that the electronic structures of  $\text{Li}_2\text{MnO}_3$  with nonzero  $J$  are qualitatively similar to the results with  $J=0$ , while the critical  $U(\text{Mn})$  for magnetic stability is increased with larger  $J$ .  $\Gamma_{2u}$  configuration is the ground state for  $U < 3$  and  $U < 4$  for  $J=0.5$  and  $0.9$ , respectively.

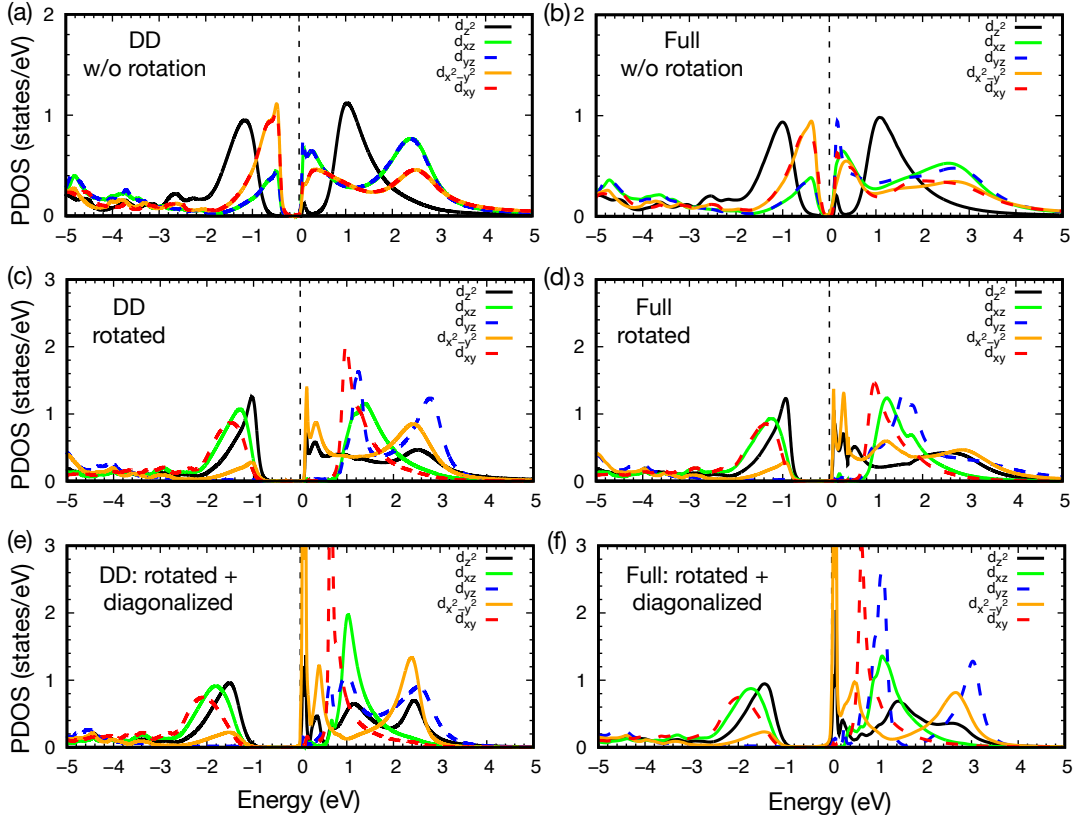


FIG. 9: DFT+DMFT spectral functions of Mn  $d$  Wannier orbitals, with  $pd$  model. (a), (c), and (e) results using density-density approximation, and (b), (d), and (f) results using full Coulomb interaction. (a), (b) global coordinate is used for Wannier projection, (c), (d) local coordinate obtained by unitary rotation matrix is used for Wannier projection, and (e), (f) block diagonal part of Mn  $d$  Hamiltonian is diagonalized. The calculations use  $U = 5$  eV,  $J = 0.9$  eV, and a temperature of 300 K.

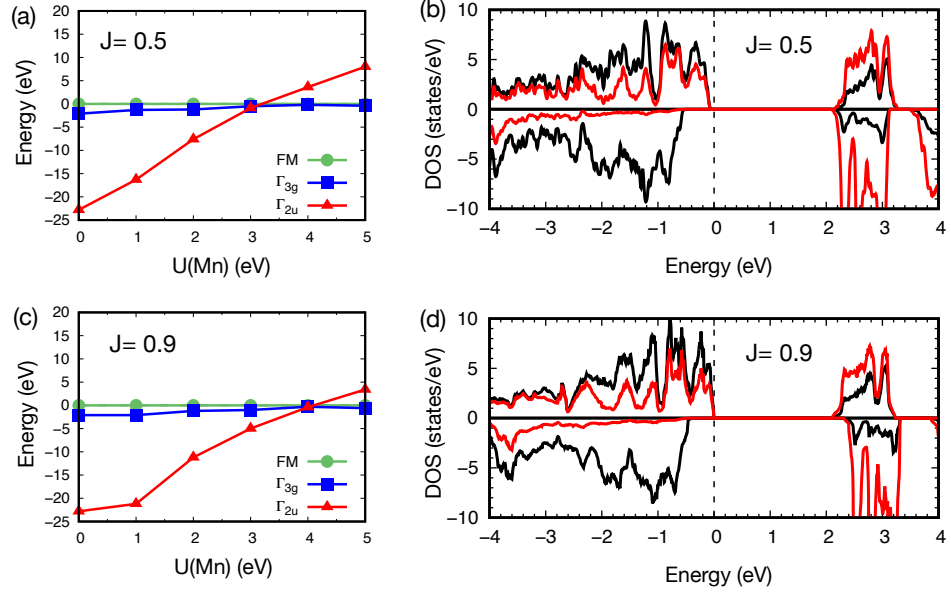


FIG. 10: The relative energies of the ferromagnetic,  $\Gamma_{2u}$ , and  $\Gamma_{3g}$  phases, as a function of  $U(\text{Mn})$  when (a)  $J=0.5$  and (c)  $J=0.9$ . Energy of the ferromagnetic phase is set to be zero. Projected density of states (PDOS) onto the Mn  $d$  (red) and O  $p$  (black) in  $\text{Li}_2\text{MnO}_3$  with  $U(\text{Mn})=2$ , using (b)  $J=0.5$  and (d)  $J=0.9$ .